Physicochem. Probl. Miner. Process., 62(7), 2026, 223969

http://www.journalssystem.com/ppmp

Physicochemical Problems of Mineral Processing

ISSN 1643-1049

Gas-assisted control of arch stability in bulk material discharge

Saule Kazhikenova, Sandugash Akhmetova

Abylkas Saginov Karaganda Technical University

Corresponding author: s.kazhikenova@ktu.edu.kz (Saule Kazhikenova)

Abstract: This study investigates the effect of gas velocity, direction, and configuration on arch formation and collapse during bulk granular material discharge through horizontal orifices. Experiments were conducted using cold quasi-2D (250 × 50 × 5 mm) and hot scale models (cylindrical shaft, D = 300 mm, H = 500 mm) with high-speed imaging (2000 fps, 1280 × 1024) across various materials. Uniform gas flow stabilizes arches, reducing the normalized mass flow rate Z_t/Z_0 to 0.20 ± 0.03 at critical gas velocity ratios $W_1/W_2 \leq 20$ and area ratios $L_1/L_2 \geq 0.37$. Conversely, localized gas jets increase Z_t/Z_0 to 1.45 ± 0.05. The scientific novelty lies in developing a unified torque-balance model that, for the first time, predicts critical counter-current gas velocities W_{kr} across different configurations within a ±28.9% error margin (n = 3, p < 0.05). These findings provide a quantitative basis for designing industrial systems such as shaft furnaces, pneumatic conveyors, and dosing units. Future work will focus on industrial-scale validation, extension to humid or adhesive materials, and complex geometries to further optimize gas-assisted flow control.

Keywords: bulk materials, torque balance, dynamically unstable arches, granular flow, shaft furnacel

1. Introduction

The discharge of bulk granular materials through horizontal conduits remains a significant challenge in industrial applications due to the unpredictable formation of arches, intermittent flow, and sudden blockages. While vertical gravity-driven hopper systems are relatively well understood, horizontal configurations present additional complexities, particularly when counter-current or co-current gas flows are introduced. These gas-solid interactions can stabilize or destabilize arch structures, significantly altering mass flow rates and potentially causing complete flow stoppage. Despite its practical importance, the precise mechanisms governing transitions between continuous, pulsating, and blocked flow under varying gas-dynamic conditions are not fully understood, limiting the predictive capability of traditional empirical or continuum-based models. Existing models, such as (Chu et al., 2022; Ma et al., 2022; Huang et al., 2024) based simulations, often fail to capture particle-scale interactions and the dynamic formation and collapse of arches, which are the key controlling factors in horizontal discharge systems. Without a physically grounded framework, engineers are forced to rely on trial-and-error or overly conservative design approaches, leading to inefficient material handling, increased downtime, and higher operational costs. Therefore, a systematic experimental and theoretical investigation is required to quantify how gas velocity, flow direction, and outlet geometry influence arch stability, mass flow rates, and critical flow transitions.

Previous studies have largely focused on gravity-driven hopper flows and vertical discharge systems, using empirical correlations, e.g., Beverloo-type models (Kobylka et al., 2021; Alonso-Marroquin and Mora, 2021) or continuum-based numerical simulations, such as Reynolds-Averaged Navier-Stokes (RANS) (Wang et al., 2023; Wang et al., 2017) and unsteady RANS methods (Zhang et al., 2022; Guo et al., 2026; Chen et al., 2023). However, transitions among continuous flow, pulsating discharge, and clogging remain inadequately characterized, especially in horizontal configurations with counter-current gas flows. Recent CFD-DEM studies have demonstrated that particle interactions, agglomeration, and aerodynamic resistance significantly influence granular flow behavior (Xie et al., 2021; Chen et al., 2024; Tang et al., 2024; Wang et al., 2025). These studies provide valuable insights into

DOI: 10.37190/ppmp/223969

particle-scale mechanisms, but a comprehensive framework linking arch stability, gas flow configuration, and microstructural dynamics in horizontal systems remains absent. Incorporating CFD-DEM insights into the theoretical framework strengthens the prediction of flow transitions, critical velocities, and arch collapse mechanisms (Qiu et al.,2024; Li et al., 2024; Zhu et al., 2024).

To address this research gap, the present study investigates gas-assisted control of arch stability in horizontal discharge systems. Cold (250 × 50 × 5 mm, quasi-2D) and hot (D = 300 mm, H = 500 mm) scale models were employed to systematically vary gas velocity, direction, and distribution, while recording particle motion with high-speed imaging (2000 fps, 1280 × 1024) and gravimetric measurements (±50 mg). Experimental materials included millet, limestone, agglomerates, and pellets, covering a wide range of particle sizes (0.4-15 mm), bulk densities (14.3-39.3 kN/m³), and porosities (0.43-0.56). The study integrates these observations with a torque-balance framework for dynamically unstable arches to provide a physically consistent model for predicting mass flow rates, arch collapse frequency, and critical gas velocities under diverse operating conditions. This approach addresses the limitations of purely empirical and continuum models, offering both theoretical insight and practical guidance for industrial systems.

To clearly highlight the advantages and uniqueness of this study, a comprehensive comparison with baseline literature and modern numerical models is established. While classical works focus primarily on gravity-driven hopper discharge without gas interactions, and numerical approaches face high computational costs, the present study bridges this gap. Specifically, we integrate a torque-balance theory with high-resolution experiments to provide accurate, physically consistent predictions across a broad parametric range.

The major differences in modeling approaches, system limitations, and identified flow regimes are systematically summarized in Table 1.

Table 1. Comparison of the present study with previous works

Study	System	Gas-solid interaction	Flow description	Arch mechanism	Modeling approach	Key limitation	Main focus
Beverloo et al.	Hopper discharge	No	Gravity flow	Not considered	Empirical scaling	No gas effects	Discharge rate
Nedderman et al.	Granular flow in silos	Limited	Continuum flow	Indirect	Continuum model	No micro-mechanism	Flow prediction
CFD–DEM studies (2020–2026)	Pneumatic systems	Yes	Particle-scale flow	Implicit	CFD–DEM coupling	High computational cost	Local flow structures
Present study	Horizontal outlet system	Yes	Arch + circulation regimes	Explicitly considered	Torque-balance framework + experiments	Extension to industrial scale required	Gas-controlled arch stability and regime transition

2. Materials and methods

The structural stability of a dynamically unstable arch located above the discharge orifice is governed by the rotational dynamics of interacting particles. Arch collapse occurs when the torque generated by frictional forces exceeds the resistance to particle rolling.This stabilization extends the lifespan of the vault, consequently reducing the mass flow rate of the granular medium (Amanbaev and Antony, 2022; Xu et al., 2026; Zhang et al., 2024).

The torque B_1 responsible for the rolling of two adjacent particles within a dynamically unstable arch during gravity-driven discharge can be defined by Equation (1)

$$B_1 = T_1 h_1 - T_2 h_2. \quad (1)$$

Assuming uniform particle radii $h_1 = h_2 = h$, Equation (1) can be simplified as Equation (2)

$$B_1 = T_1\left(1 - \frac{T_2}{T_1}\right)h, \tag{2}$$

where T_1 and T_2 represent the frictional forces between neighboring particles.

Under counter-current gas flow conditions, an additional aerodynamic force G acts on the arch structure. The modified torque is then expressed by Equation (3)

$$B_2 = T_1\left(1 - \frac{T_2+G}{T_1+G}\right)h. \tag{3}$$

This mathematical framework for granular mass flow, supported by 2K/3K numerical simulations, has demonstrated high predictive accuracy across a wide range of orifice geometries (Mankoc, et al., 2007). Furthermore, the oncoming gas flow acts as a braking mechanism for particles descending from the arch. As the gas velocity increases such that the ratio $\frac{T_2+G}{T_1+G} \to 1$, the resulting torque B_2 approaches zero, leading to a complete cessation of material discharge. This state is further stabilized by the gas flow providing upward support to the particles, which prevents their rotation and effectively causes layer hanging (Amanbaev and Antony, 2022). Conversely, in systems characterized by a co-current gas flow (moving in the same direction as the material layer), an increase in gas velocity modifies the force balance such that the ratio $\frac{T_2-G}{T_1-G}$, decreases. To investigate the micro-mechanisms of granular flow and arch dynamics, a specialized flat transparent model was utilized. The geometric characteristics of the experimental apparatus are schematically illustrated in Fig. 1. The main body features a rectangular upper section filled with a granular bed and a conical hopper bottom with a half-angle of θ. The material discharges through a bottom orifice under the action of gravity, establishing a downward granular flow direction. To manipulate the arch dynamics and flow behavior, gas is introduced into the lower section via gas injection nozzles, generating a localized gas injection vector into the bed.

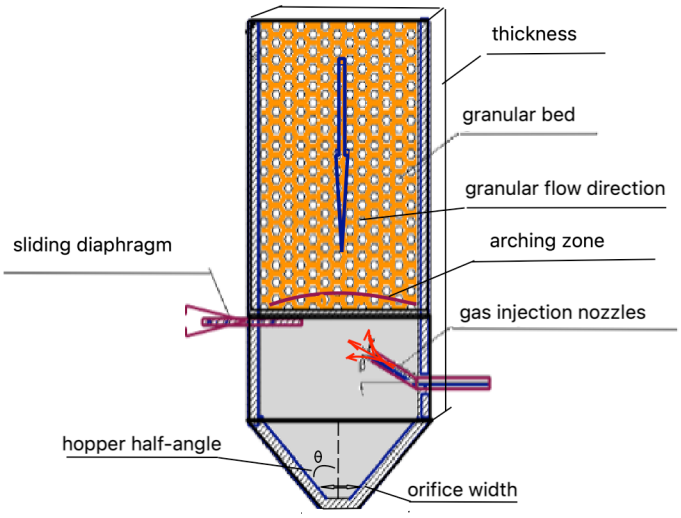

Fig.1. Schematic representation of the quasi-2D transparent model used for granular flow visualization

2.1. Cold model (Quasi-2D)

The experimental procedure involved the following technical specifications:

- **Gas sources and calibration**

High-purity bottled gases, including hydrogen (H_2, 99.999% purity, 5.0 grade) and helium (He, 99.995% purity, 4.5 grade), were utilized in the cold-model experiments. Prior to injection, all gases were filtered to remove particulate contaminants and subsequently dried to a dew point of -40 °C to eliminate moisture effects in the gas supply lines. Gas flow rates up to 60 m³/h were regulated using RS-type rotameters with a measurement uncertainty of ±3%. These flowmeters were individually calibrated for each working gas (H_2, He, air) against reference flow standards traceable to the National Institute of Standards and Technology (NIST). Calibration curves were constructed over the full operating range, applying linear interpolation between calibration points, and verified prior to each experimental series to ensure traceable and reproducible gas-flow measurements.

- **Experimental geometry and similarity conditions**

A transparent quasi-two-dimensional model with dimensions of 250 × 50 × 5 mm was employed to provide optical access for high-speed imaging. The granular bed height was maintained at 200 ± 3 mm. The discharge system included a replaceable diaphragm with outlet diameters ranging from 10 to 60 mm. The shaft was vertically mounted above a receiving bin with a height of 800 mm, diameter 250 mm. To ensure valid gas-dynamic and granular scaling, geometric similarity conditions were strictly satisfied according to the following criteria: $\frac{D_{shaft}}{d_p} > 20$, $\frac{D_{outlet}}{d_p} > 5$, $\frac{H_{bed}}{D_{shaft}} \geq 2$, where D_{shaft} is the shaft diameter, D_{outlet} is the outlet diameter, d_p is the equivalent particle diameter, and H_{bed} is the bed height. The outlet-to-shaft diameter ratio was systematically varied from 0.1 to 0.7.

- **Gas injection and granular materials**

Gas was introduced into the system either as a uniform flow or as concentrated jets through three identical stainless-steel nozzles located 30 mm below the outlet. The nozzles featured an internal diameter of 8 mm, a length of 20 mm, a circular smooth-edged outlet configuration, and were oriented at an angle of 90° relative to the shaft axis. The granular bed was composed of distinct bulk materials, specifically millet, limestone, and agglomerate particles, allowing for a comprehensive analysis of physical property effects on flow behavior.

- **Reproducibility, statistics, and environmental control**

To ensure the reliability of the experimental data, each test was repeated 3 times (n = 3), and the results are reported as the mean value ± the standard deviation. The system demonstrated high reproducibility, with the coefficient of variation for the mass flow rate remaining strictly below 5%, and the total measurement uncertainty confined to less than 6%. Environmental conditions within the laboratory were continuously regulated and maintained at a temperature of 22 ± 2°C and a relative humidity range of 45–55% throughout all testing series.

- **Characterization of granular materials**

Experiments were conducted using millet, limestone, and agglomerate fractions with particle sizes ranging from 1.45 to 2.44 mm. To ensure reproducibility, key material properties were systematically measured before each experimental series. The moisture content was determined by oven drying at 105°C for 24 h and remained strictly below 1% for all investigated materials. The particle shape factor (sphericity) was evaluated via digital image analysis, yielding values between 0.65 and 0.95 depending on the specific material type. The angle of repose was determined using the standard tilting-box method, ranging from 28° to 38°C. Furthermore, the particle size distribution was verified by a combination of sieve analysis and laser diffraction methods. Consequently, the selected materials covered a broad range of density, porosity, permeability, and frictional characteristics.

- **High-speed imaging system**

The dynamics of stable arch formation and destruction were recorded using a high-speed SK-16 camera operating at a frame rate of 2000 fps with a spatial resolution of 1280 × 1024 pixels. To provide optimal contrast for particle tracking, a uniform LED backlighting system was utilized. The camera was positioned strictly perpendicular to the quasi-two-dimensional plane of the flat transparent model to eliminate parallax effects and minimize geometric distortions during image processing.

- **Experimental procedure**

The granular bed was filled under gravity without vibration to ensure reproducible packing conditions. The shaft was hermetically sealed prior to each experiment, and a prescribed gas flow rate was established using calibrated RS-type rotameters before initiation of material discharge. Discharge was triggered by opening the regulating diaphragm, while the receiving hopper remained sealed during the measurement period. The mass flow rate Z was determined gravimetrically from the collected material in the receiving bin over a fixed time interval with a measurement precision of ±50 mg. The pressure drop ΔP acting on the granular arch was calculated from the difference between gas pressures measured above and below the discharge outlet using flush-mounted pressure taps and U-shaped manometers.

Flow-regime transitions and arch dynamics were simultaneously recorded using a high-speed imaging system, enabling frame-by-frame analysis of granular motion and structural collapse events.

Experimental observations indicated that stable cyclic discharge occurs under the following conditions: $\frac{W_1}{W_2} \leq 20$ and $\frac{L_1}{L_2} \geq 0.37$, where W_1 is the gas velocity through the nozzle; W_2 is the gas velocity at the outlet; L_1 is the outlet area; L_2 is the cross-sectional area of the gas jet at interaction with the material surface. High-speed image analysis showed that increasing gas velocity reduced the relative rolling velocity of particles within the arch region, resulting in lower mass discharge rates. Both counter-current and co-current flows exhibited cyclic formation and destruction of dynamically unstable arches. Increasing counter-current gas velocity reduced the frequency of arch collapse and could ultimately cause complete flow stoppage, whereas co-current flow enhanced material discharge.

2.2. Hot model (thermal–gas–dynamic system)

- **Gas supply, measurement, and flow regimes**

The gas supply system for the hot model utilized the same high-purity gases as the cold-model setup, specifically hydrogen (H_2, 99.999%), helium (He, 99.995%), and dried compressed air featuring a dew point of -40°C). Gas flow rates up to 60 m³/h were monitored using RS-type rotameters calibrated to NIST-traceable standards, delivering an operational accuracy within ±3%. System pressure profiles were captured via flush-mounted pressure taps strategically positioned along the refractory shaft walls. The operational temperature window was strictly maintained between 850°and $900°C$. Continuous temperature data were acquired at three distinct vertical positions using calibrated type-K thermocouples with an accuracy of ±2°C. A thermal steady-state was systematically verified and ensured prior to the initiation of each experimental run.

To comprehensively analyze the aerodynamic influence on stable arch formation and particle discharge mechanics under thermal conditions, two distinct operational configurations were investigated:

- A **co-current flow** regime, where both the gas phase and solid particles moved downward synchronously.
- A **counter-current flow** regime, characterized by an upward gas flow opposing the gravity-driven downward motion of the solids.

- **Experimental procedure**

The furnace shaft was hermetically sealed prior to each experiment. A prescribed gas flow rate was established using calibrated RS-type rotameters before the initiation of material discharge. Material discharge was initiated by opening the regulating outlet system after the stabilization of gas flow conditions. The mass flow rate Z was determined gravimetrically from the collected material in the receiving bin over a fixed time interval with a precision of ±50 mg. The pressure drop ΔP was measured as the difference between gas pressures recorded at upper and lower positions of the shaft using flush-mounted pressure taps and U-shaped manometers. Both gas flow rate and pressure distribution were continuously monitored during operation. Flow conditions were analyzed under both co-current and counter-current regimes to evaluate their influence on gas-solid interaction and discharge stability.

- **Reproducibility**

Each condition was repeated 3 times. Results are reported as mean ± standard deviation. Mass flow CV remained <5%. Temperature fluctuations during steady state did not exceed ±2°C.

The combined experimental framework ensures full geometric and dynamic similarity control, traceable gas-flow calibration, quantified uncertainty (<6%), statistically validated repeatability (n=3), reproducible granular packing conditions, synchronized pressure-flow-visual measurements (cold model), thermally controlled gas-solid interactions (hot model). Statistical analysis of the experimental data was performed using Microsoft Excel. All measurements were carried out in triplicate (n=3). Quantitative data in the text and tables are expressed as the mean value standard deviation ($M \pm SD$). For the graphical representations (Figs. 6–11), data points are plotted as the mean values with error bars representing the standard error of the mean ($M \pm SEM$). The statistical reliability of the empirical error ranges was validated by calculating 95% confidence intervals based on Student's t-distribution.

Cold model experiments were used to investigate gas-solid hydrodynamics under isothermal conditions, ensuring full geometric and dynamic similarity, traceable gas-flow calibration, quantified uncertainty (<6%), statistically validated repeatability (n=3), and reproducible granular packing. Synchronized pressure–flow–visual measurements were performed to capture flow structure evolution.

Gas with properties listed in Table 2 was supplied at flow rates up to 60 m³/h through three symmetrically arranged pipes (8 mm in diameter), providing uniform gas distribution across the material bed.

Analysis of high-speed filming data from the cold model reveals that an increase in gas velocity leads to a significant reduction in the relative rolling velocity of particles within the arch, which correlates with a decrease in the overall mass discharge rate (Lu et al., 2024).

Across the investigated range of pressures and gas velocities, the discharge mechanism retains a staged nature, characterized by cyclic formation and destruction of dynamically unstable arches.

The mechanism of bulk material flow summarized in Table 3 is derived from observations in the cold model experiments, describing the qualitative behavior of the system under different flow regimes.

Table 2. Physical properties of the investigated gases

Gas Type	Specific Gravity, N/m³	Dynamic Viscosity 10^{-5} Pa· s
Hydrogen	1.17	0.88
Helium	1.58	1.94
Air + 62% Helium	5.48	1.88
Air + 34% Helium	8.45	1.87
Air	11.96	1.82

Table 3. Mechanism of bulk material flow

Flow Mode	Frequency of Vault Failure	Discharge Rate	System Status
Gravitational (Base)	Baseline	Standard	Stable
Counter-current (↑)	Decreasing	Falling	Risk of hanging
Co-current (↓)	Increasing	Intensive	Enhanced flow

Visual observations confirmed that as the counter-flow velocity increases, a critical threshold is reached where the frequency of arch failure becomes minimal, leading to a complete cessation of discharge. Conversely, co-current flow consistently demonstrated higher discharge velocities across the entire pressure range, supporting theoretical calculations regarding the aerodynamic contribution to particle rolling dynamics (Sun et al. 2025). To ensure scalability of laboratory results to industrial conditions, similarity criteria were strictly maintained, allowing extrapolation from cold model observations to hot model operation (Zhanxia, et al., 2025; Xu, et al., 2024). Experiments involve setting a prescribed gas flow rate and initiating discharge by opening the regulating damper. The mass flow rate (Z) is determined by gravimetric analysis of the material collected in the sealed receiving bin or model furnace over a fixed time interval (Wu, et al., 2024).

The investigations utilized both cold and hot laboratory models (Figs. 2 and 3).

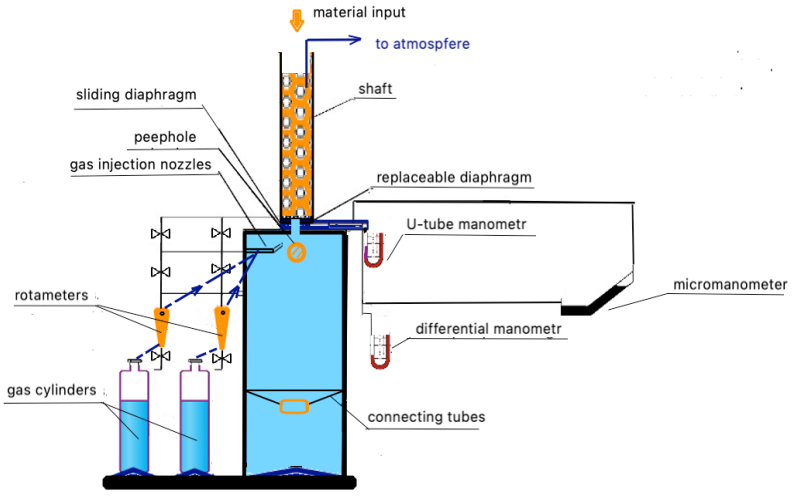

Fig. 2. Schematic layout of the experimental apparatus for granular flow and gas injection testing

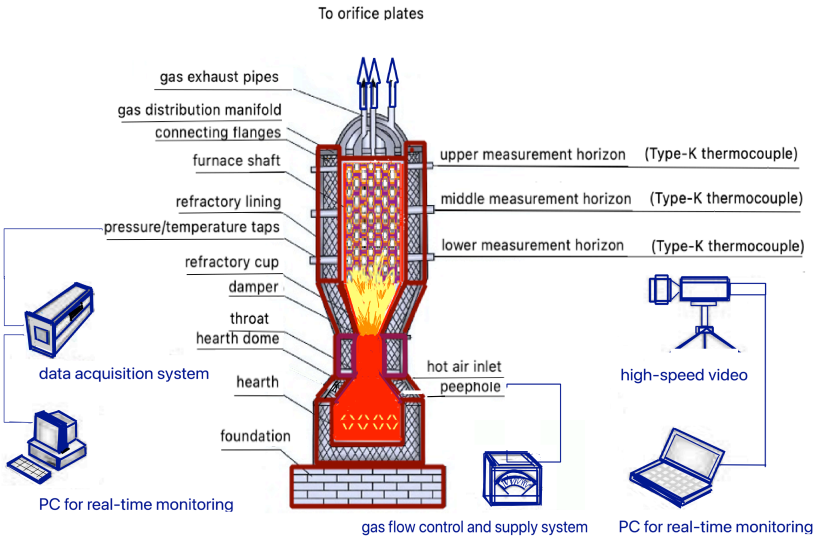

Fig. 3. Schematic diagram and structural components of the enlarged refractory-lined hot model

The hot laboratory model (Fig. 3) was developed to simulate thermal-gas-dynamic conditions. It features a modular design consisting of steel sections lined with fireclay bricks for thermal insulation. To maintain system airtightness under elevated temperatures, detachable joints were sealed with specialized asbestos gaskets.

The physical properties of the gases and granular materials used in the experimental series are summarized in Table 4.

Table 4. Characteristics of bulk materials

Material	Fraction, mm	Equiv. Diameter 10^{-3}, m	Friction Coefficient	Bed Porosity, m^3/m^3	Apparent Specific Gravity 10^3, N/m^3
Agglomerate I	3.0–10.1	5.49	0.68	0.49	35.50
Agglomerate II	3.4–4.6	4.05	0.68	0.54	37.38
Agglomerate III	1.6–2.6	2.01	0.66	0.53	36.91
Millet	1.6–2.6	2.01	0.56	0.43	14.35
Limestone I	2.5–3.7	3.09	0.58	0.48	25.68
Limestone II	0.4–1.1	0.65	0.57	0.46	27.47
Coke	1.6–2.6	2.01	0.96	0.56	16.22
Pellets I	5.0–15.1	8.67	0.59	0.52	39.25
Pellets II	4.0–6.1	4.91	0.61	0.55	38.76

2.3. Calibration procedure

Gas flow rates were measured using RS-type rotameters individually calibrated for hydrogen, helium, and air using NIST-traceable reference standards. Calibration curves were constructed over the operating range of 0-60 m^3/h. The measurement uncertainty did not exceed ±3%, and calibration was verified before each experimental series. Fig. 4 and Table 5 show the calibration characteristics of the RS-type rotameter for H_2, He, air. The calibration curve was fitted using a linear regression model $\Phi = a\mathcal{R} + b$, where Φ actual volumetric flow rate (m^3/h), $\mathcal{R}$ rotameter reading (divisions).

- Air: $\Phi = 1.2457\mathcal{R} - 11.235 (\mathcal{R}^2 = 0.9874)$.
- Helium: $\Phi = 1.1575\mathcal{R} - 10.572 (\mathcal{R}^2 = 0.9844)$.
- Hydrogen: $\Phi = 1.072\mathcal{R} - 9.8446 (\mathfrak{R}^2 = 0.9856)$.

The experimental data exhibited a nearly linear dependence between the rotameter indication and the actual gas flow rate. Linear regression analysis confirmed excellent agreement between the measured and predicted values, with coefficients of determination approaching unity.

Table 5. Calibration data of RS-type rotameters for air, helium, and hydrogen.

Rotameter reading (m^3/h)	Air actual flow (m^3/h)	Helium actual flow (m^3/h)	Hydrogen actual flow (m^3/h)
0	0.0	0.0	0.0
10	10.2	9.4	8.8
20	20.5	18.9	17.6
30	30.8	28.5	26.5
40	41.0	38.2	35.4
50	51.3	47.8	44.2
60	61.5	57.2	53.0

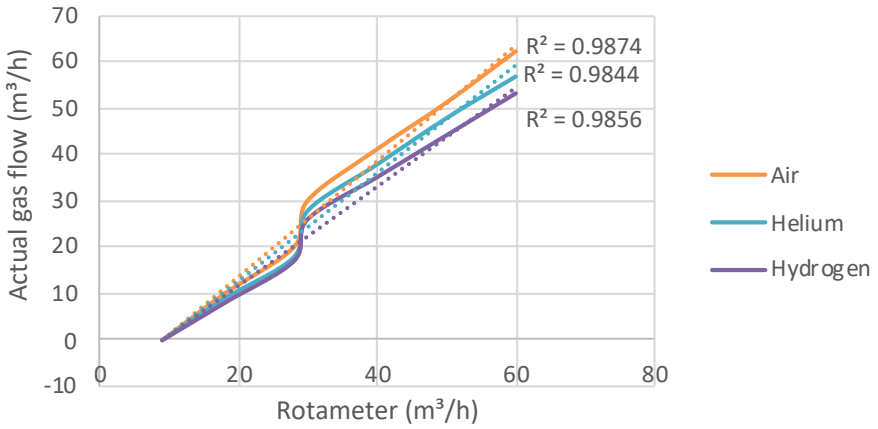

Fig.4. Linear calibration curves of the RS-type rotameter for air, helium and hydrogen

During the preparation and execution of the experiments, the exhaust port was secured using a lined damper with specialized orifices for gas passage. A hermetically sealed hatch located in the furnace hearth managed the material discharge process. The furnace operation involves a forced air supply (blast) into the fuel combustion zone to rapidly achieve and maintain the required operating temperatures (Wu, et al., 2024). Compressed air was supplied to the scale model from the factory line, while hydrogen was provided via high-pressure cylinders.

The experimental investigation evaluated several gas supply configurations to determine their impact on granular flow stability (Fig. 5). The complete flow blockage of the bulk material was identified by three simultaneous indicators: a sharp escalation in the gas pressure drop, the cessation of pulsations in the pressure gauge working fluid, and direct visual confirmation through observation ports.

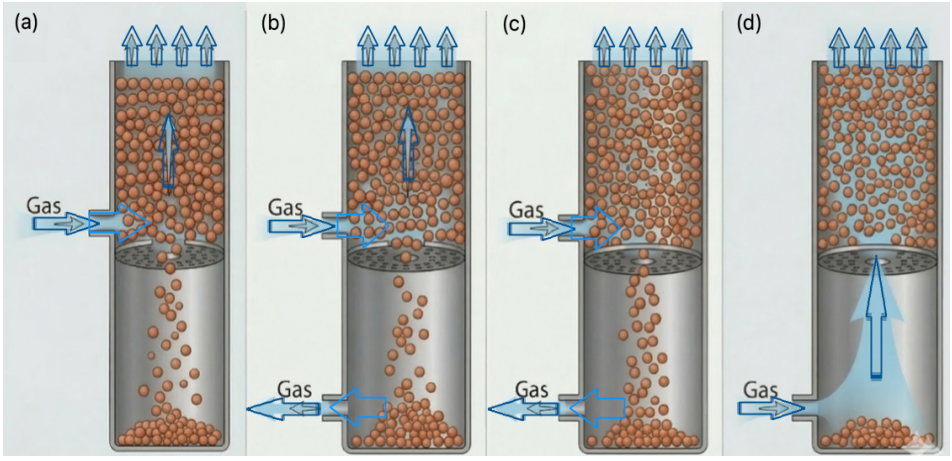

Fig. 5. Gas supply configurations for the experimental model positioned above the outlet with: (a) the top open and bottom closed; (b) both top and bottom boundaries open; (c) the top closed and bottom open; (d) below the outlet with the top of the model open

Based on the measured gas pressure difference above and below the discharge orifice, the effective pressure drop acting on the dynamically unstable arch was calculated by Equation (4)

$$\Delta P_0 = \Delta P \cdot \frac{s_{eq}}{m_0}, \tag{4}$$

where ΔP is the measured pressure drop across the granular bed; s_{eg} is the equivalent particle diameter; m_0 is the characteristic height of the granular layer.

For engineering analysis of gas-assisted granular discharge, the mass flow rate F (kg/s) can be expressed in terms of local flow conditions. The volumetric discharge rate is commonly expressed byEquation (5):

$$F = \mu S \rho v, \tag{5}$$

where μ is the discharge coefficient, S is the cross-sectional area, ρ is the gas density, and v is the flow velocity.

For pressure-driven outflow, the mass flow rate can also be described by the classical orifice Equation (6):

$$F = C_s A \sqrt{2\rho\Delta P} \tag{6}$$

where C_s is the empirical flow coefficient, A is the orifice area, and ΔP is the pressure drop.

3. Results

The obtained results indicate that gas flow direction and velocity are the key factors governing the stability of dynamically unstable arches and the resulting discharge regimes of bulk materials. Experimental observations obtained using the cold scale model (Figs. 5 and 6) demonstrate that the gas supply configuration strongly influences the discharge dynamics.

When gas is supplied above the discharge orifice and evacuated through the upper boundary of the model (Fig. 5(a)), its influence on the solid mass flow rate is negligible. This behavior is illustrated by Fig. 6(a), where the ratio Z_t/Z_0 remains close to unity over the entire investigated range of gas flow rate H_r/H_{kr}.

The experimental results illustrating the dependence of the target parameter Z_t/Z_0 on the variable H_r/H_{kr} across five different operational modes (a)-(e) are presented in Fig. 6 and Table 6. The obtained curves reveal distinct dynamic trends depending on the selected mode. Specifically, modes **(**c) and (*d)* exhibit a monotonic increase, reaching their maximum values at $\frac{H_r}{H_{kr}} = 4$. In contrast, modes **(**a) and (b) remain stable and demonstrate virtually no variation across the entire investigated range, indicating the stability of the system under these conditions. Conversely, mode (e) shows a pronounced linear decline, dropping to a final value of $0.31 \pm 0{,}05 (M \pm SD)$. Crucially, the non-overlapping boundaries of the 95% confidence intervals (CI) for modes (c), (d)**,** and **(**e**)** at $\frac{H_r}{H_{kr}} > 1$ clearly confirm the statistical significance of the observed differences. The clear separation between these empirical error zones demonstrates that the variation in operational modes leads to mathematically reliable changes in the system's behavior.

Table 6. Representative experimental dataset and statistical processing parameters for operational mode (a) (corresponding to Fig. 6(a))

Z_t/Z_0	H_r/H_{kr1}	H_r/H_{kr2}	H_r/H_{kr3}	Mean	SD	SEM	CI
0	1	0,999	1	0.999667	0.0005774	0.000333	0.001434
0.24	1	1	0.999	0.999667	0.0005774	0.000333	0.001434
0.6	1	1	0.999	0.999667	0.0005774	0.000333	0.001434
1.3	0.995	0.992	0.99	0.992333	0.0025166	0.001453	0.006252
2	0.99	0.99	0.995	0.991667	0.0028868	0.001667	0.007171
2.7	0.98	0.982	0.988	0.983333	0.0041633	0.002404	0.010342
4	0.97	0.972	0.971	0.971	0.001	0.000577	0.002484

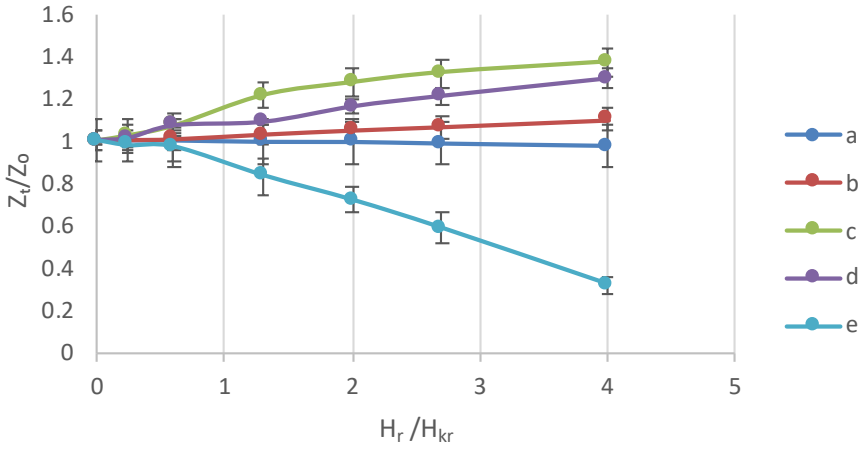

Fig. 6. Target parameter Z_t/Z_0 as a function of H_r/H_{kr} for various operational modes (a)-(e). Data points represent the mean values, and vertical error bars indicate the standard error of the mean (SEM, n=3)

To illustrate the experimental error estimation and data reduction workflow, a representative primary dataset corresponding to operational mode (a) is summarized in Table 6. This table details the raw triplicate measurements, calculated arithmetic means, standard deviations (SD), standard errors of the mean (SEM), and 95% confidence intervals (CI) across the investigated range of the Z_t/Z_0 parameter. The statistical processing, error analysis, and boundary calculations for all other experimental regimes and curves depicted in Figs. 6–11 were performed in an identical manner.

In contrast, the configuration involving gas extraction through both the top of the model and the receiving hopper (Fig. 5(b)) exhibits behavior strongly dependent on bed porosity. For highly porous materials, the influence of the gas phase remains limited (Fig. 6(b)). However, as porosity and gas permeability decrease, a larger fraction of the gas stream is forced through the discharge outlet. This results in a significant intensification of the material flow rate (Fig. 6(d)), attributed to the additional downward aerodynamic force acting on particles in the orifice region.

When the gas is supplied above the outlet and subsequently removed through it (Fig. 5(c)), a clear correlation is observed: the mass flow rate increases proportionally with the gas flow rate and the local pressure gradient (Fig. 6(c)). These findings are in strong agreement with previously reported studies (Barletta, et al., 2003).

The fundamental mechanism behind these observations lies in the interaction between the gas phase and the dynamically unstable arch (vault) formed at the outlet. Variations in the gas supply volume and the resulting pressure within the bulk layer directly modify the stability of this arch. Excess pressure above the material layer imposes a supplementary vertical load, which increases the frequency of arch destruction (Scheffler and Coetzee, 2023; Bembenek et al., 2024). Consequently, this leads to an increase in the initial velocity of particles following structural failure, ultimately resulting in a higher total mass velocity of the material outflow.

Notably, Fig. 6(e) illustrates the regime of counter-current flow, where gas introduction below the outlet leads to a rapid reduction in the discharge rate until complete material blockage occurs as $H_r/H_{kr} \rightarrow 1$ due to the stabilization of the arch structure.

The observed extremum in the dependence of the mass flow rate on the volume of air supplied is primarily attributed to the spatial positioning of the nozzle relative to the discharge orifice. The distance between the air injection point and the outlet directly determines the kinetic energy delivered to the surface of the dynamically unstable arch. This energy transfer regulates the frequency of structural failure and, consequently, the material outflow velocity. These observations are consistent with existing experimental data regarding nozzle positioning effects (Hanif, et al., 2025). As the air flow rate and velocity increase, a stable air channel tends to develop within the granular bed, extending directly through the outlet. This channel formation fundamentally alters the transport mechanism. However, a subsequent decrease in the mass flow rate can occur due to the local compaction of the material surrounding the concentrated air stream. The probability of such channeling is notably higher in materials with greater bed density. Furthermore, at relatively small outlet diameters and elevated

overpressures (ranging from 9.8 to 29.4 kPa), the compaction effect and gas-induced stabilization of the arch can lead to a complete cessation of discharge.

A rigorous comparison was conducted between the obtained experimental data (for gas supply Fig. 5(b) and 5(c)) and traditional empirical mass flow rate equations. The results reveal substantial discrepancies, with calculated errors fluctuating across a remarkably wide range specifically from -25.1% to +47.1%, -32.6% to +55.7%, and +9.1% to +79.1%, respectively.

When gas is introduced below the discharge zone (Fig. 5(d)), the mass flow rate of various granular media gradually diminishes from 60% to 20% of the baseline gravity discharge rate. A further escalation in the gas flow velocity leads to a total cessation of material discharge, as illustrated by Fig. 6(d). This broad spectrum of flow regulation limits is primarily attributed to the diverse physical and mechanical attributes of the investigated materials (Banik, et al., 2024). Key factors such as particle size distribution, moisture content, adhesion forces, and electrical properties significantly influence the interaction between the gas phase and the granular assembly.

Further evaluation shows that the average error for empirical predictions is approximately ±40%, with localized deviations reaching as high as +176.0% or dropping to -100.0%. These inaccuracies intensify sharply as the gas velocity approaches the critical threshold for flow blockage. Such results underscore that classical empirical models are inadequate for describing gas-solid systems where internal structural dynamics are dominant.

To overcome the limitations of classical empirical models and explain the underlying phenomena, the internal structural and mechanical properties of the materials must be considered (Table 4). Specifically, the difference in Z_t/Z_0 kinetics for millet (*a*) and agglomerate III (*b*) with identical particle sizes (2.01 mm) is due to the fact that agglomerate III is 2.5 times heavier than millet, $36.91 \cdot 10^3$ compared to $14.35 \cdot 10^3 N/m^3$. High inertia stabilizes the agglomerate bed up to $H_r = 0.7 m^3/h$, after which the critical gas pressure causes an exponential elutriation of particles (*b*), whereas lightweight millet particles are entrained uniformly (a).

The statistical processing and error analysis for the curves depicted in Fig. 7 were performed in an identical manner to the workflow described for Fig. 6. The calculated standard deviations (SD) and 95% confidence intervals (CI), plotted as vertical error bars, confirm high reproducibility across the entire investigated range of gas flow rates. The complete statistical datasets for these trends are omitted here, as they follow the exact reduction methodology detailed in Table 6.

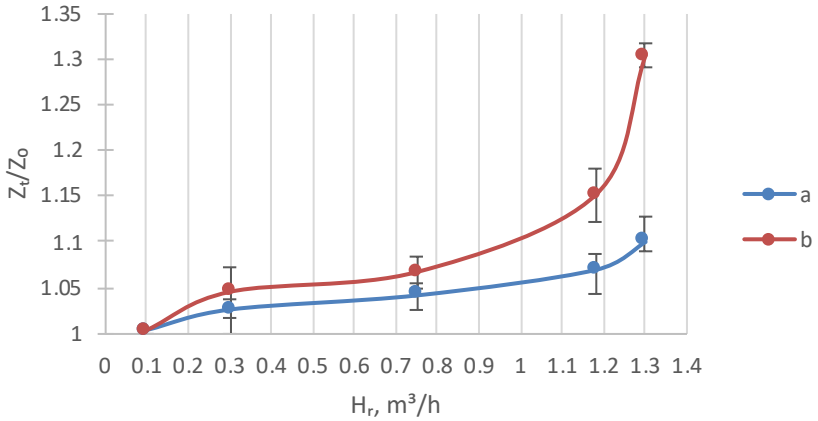

Fig. 7. Relative mass flow rate (Z_t/Z_0) as a function of gas flow rate (H_r, m³/h): (1) millet; (2) agglomerate III

Utilizing a nozzle with a reduced diameter enables the generation of high-velocity, localized gas jets (Harris and Grekova, 2005). The experimental results illustrated in Fig. 8 indicate that gas properties play a decisive role in transport efficiency.

A reduction in gas density results in a significant intensification of the material flow rate through the outlet. To evaluate the specific impacts, the effects of counter-current flows of hydrogen (c) and helium (b) were analyzed. These gases possess similar densities under the experimental conditions but exhibit significantly different dynamic viscosities. The close convergence of (b) and (c) at the initial stage, followed by their parallel separation, indicates that the impact of gas viscosity on the material

flow rate is secondary. Instead, the variation in discharge intensity is primarily governed by the gas density, which modulates the aerodynamic resistance within the arch structure.

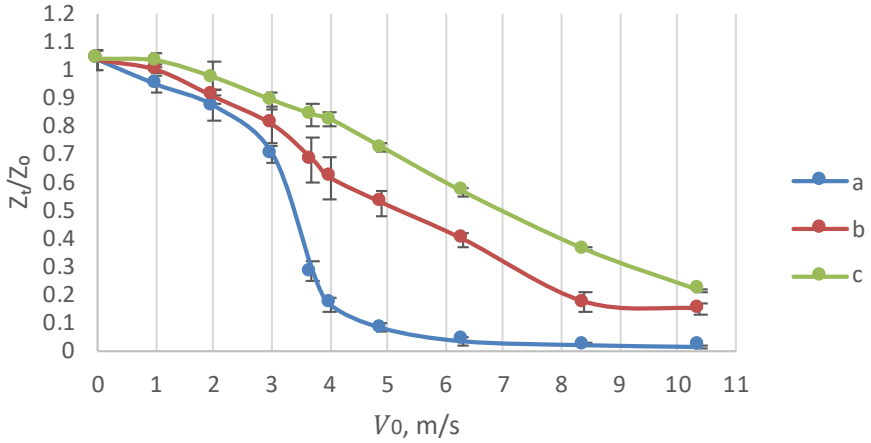

Fig. 8. Dependence of the relative mass flow rate (Z_t/Z_0) of agglomerate III on the gas velocity at the outlet (V_0, m/s) for a 30 mm orifice: (a) air; (b) helium; (c) hydrogen

This finding is of significant practical importance, as it demonstrates that the lower limit of the material mass flow rate under counter-current conditions is largely independent of the specific chemical nature or viscosity of the gas phase, provided the density remains constant. This expands the potential for implementing gas-flow-based control methods across various industrial processes, regardless of the gas composition used (Yang and Hsiau, 2001).

The sensitivity of flow regulation to the intrinsic properties of the granular medium was further evaluated in Fig. 9**.** The dependence of the relative mass flow rate (Z_t/Z_0) on the gas flow rate (H_r) shows distinct patterns for different materials: agglomerate (a), limestone (b), and millet (c), whose physical properties are detailed in Table 4**.**

The results establish that materials with lower bulk density (such as millet (c)) are more sensitive to gas-dynamic interactions, exhibiting a sharper decline in the discharge rate at lower gas flow rates. In contrast, denser materials like agglomerate (a) maintain higher flow stability, requiring significantly higher gas velocities to achieve a similar reduction in discharge. These observations confirm that the effectiveness of gas-assisted flow control is intrinsically linked to the mass-to-surface-area ratio of the particles and the resulting aerodynamic drag acting on the arch structure. To ensure data reliability, the statistical processing and error analysis for all three curves were performed in an identical manner to the workflow described for Fig. 6. The visual representation of the calculated standard deviations (SD) and 95% confidence intervals (CI) as vertical error bars demonstrates high reproducibility across the entire investigated range.

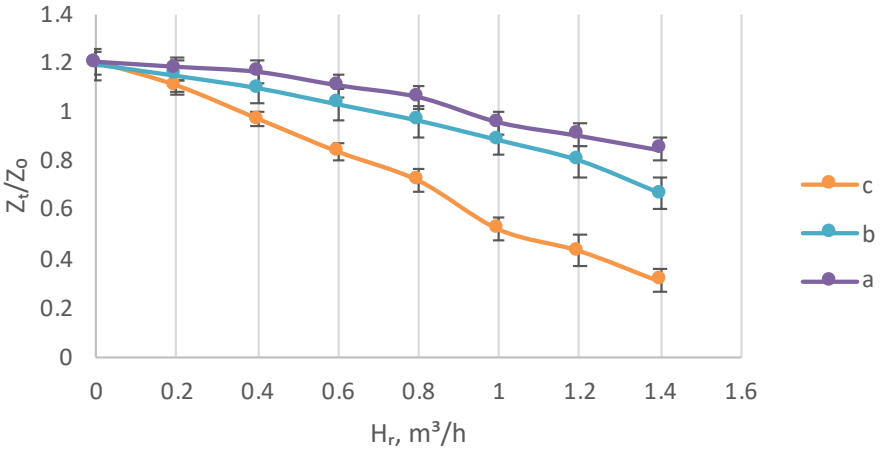

Fig. 9. Dependence of the relative material flow rate (Z_t/Z_0) on the counter-current air flow rate (H_r, m³/h) for different materials: (a) agglomerate; (b) limestone; (c) millet

The impact of particle dimensions on discharge kinetics is illustrated in Fig. 10. The dependence of the relative mass flow rate (Z_t/Z_0) on the gas flow rate (H_r) exhibits distinct patterns depending on the equivalent particle diameter (s_{eq}): larger particles (a) and smaller particles (b).

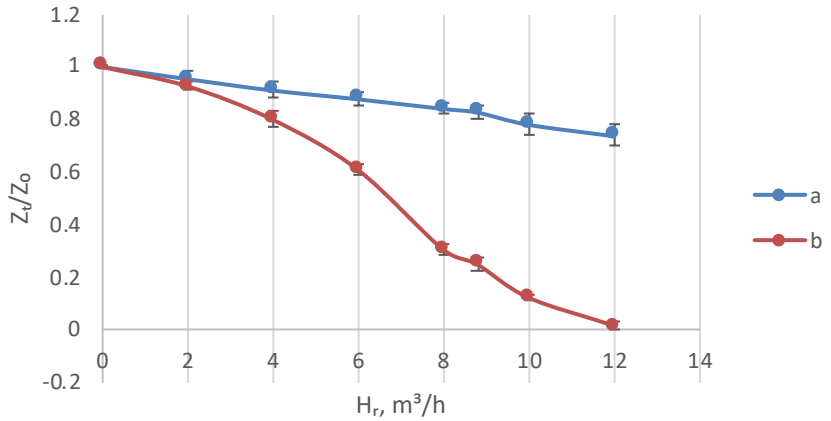

Fig. 10. Dependence of the relative pellet outflow rate (Z_t/Z_0) on the counter-current air flow rate (H_r, m³/h) for different particle sizes: (a) larger fraction (s_{eq} = 5mm); (b) smaller fraction (s_{eq} = 2mm)

As the equivalent diameter increases, a significant intensification of the mass flow rate and higher flow stability are observed. A decrease in the particle-to-outlet diameter ratio not only enhances the absolute flow rate but also extends the effective regulation range, as larger fractions resist aerodynamic drag more efficiently. To ensure data reliability, the statistical processing and error analysis for both curves were performed in an identical manner to the workflow described for Fig. 6. The calculated standard deviations (SD) and 95% confidence intervals (CI), plotted as vertical error bars, confirm high reproducibility across the entire investigated range of gas flow rates.

Mathematical analysis of the experimental data allowed for the ranking of investigated parameters based on their influence on the material discharge rate. Under standard conditions, the factors are arranged in the following descending order of significance:

1. Direction of the gas flow (counter-current vs. co-current);
2. Diameter of the discharge orifice;
3. Bulk density of the granular material;
4. Gas flow rate;
5. Physical properties of the gas (density and viscosity) (Feng and Yuan, 2021).

Notably, this hierarchy can shift under specific dynamic conditions. For instance, a 30% increase in the gas flow rate causes this parameter to exert a more dominant influence on the discharge rate than the intrinsic bulk density of the material.

To consolidate the experimental findings for both counter-current and co-current gas flow regimes, a unified empirical model was developed as Equation (7):

$$Z_t = 0.05\gamma_n \frac{D_0^{2.5}}{\sqrt{s_{eq}}} \sqrt{1 \pm \frac{\Delta P}{0.6\gamma_n D_0}}. \quad (7)$$

where gas pressure modifies the stability of dynamically unstable arch structures, resulting in either enhancement (+) or suppression (-) of discharge. The error associated with this generalized model ranges from -19.8% to +23.1%, which is significantly lower than the deviations observed when using classical empirical equations. As previously noted, traditional models exhibit errors ranging from -25.1% to +176.1%, especially near critical regimes. This confirms that the proposed Equation (7), which explicitly accounts for the gas-dynamic pressure drop ΔP and orifice geometry rate (D_0) provides a much more reliable tool for industrial design.

Comparing the experimental results with calculations of the material mass flow rate under pressure discharge using empirical equations shows that the error in the calculated values varies within a wide range, namely: from -25.1% to +47.1%, from -32.6% to +55.5%, and from +9.8% to +79.5%, respectively.

The limitations of conventional empirical models become even more apparent under counter-current gas flow conditions. For such regimes, the error in mass flow rate calculations using standard equations

escalates significantly, with deviations ranging from -21.1% to +176.1%, -99.1% to -0.7%, and -100.0% to +67.1%. On average, the predictive error is approximately ±50%. Notably, this discrepancy increases sharply when transitioning from air typically used in the baseline experiments of previous authors to gases with significantly different physical properties, such as hydrogen or helium (as detailed in Table 2). Such high levels of uncertainty underscore that purely empirical correlations, which do not account for the internal structural mechanics of the granular bed, are unsuitable for complex gas-solid systems. Consequently, there is a clear necessity for a more rigorous theoretical description of the discharge process. By integrating the results of this experimental study with the proposed torque-balance mechanism, it becomes possible to establish a physically consistent model that remains accurate across a wide range of gas-dynamic and material conditions. Equation (8) describes the dynamic discharge velocity (ω_t) as a result of the competition between gravitational driving forces and the structural resistance of dynamically unstable arches under gas-solid interaction conditions. The gas-pressure term modifies the stability of the arch structure, resulting either in suppression or enhancement of granular discharge depending on flow direction:

$$\omega_t = 0.5\sqrt{2g\mu\left[R + s\left(0.5 + \frac{1-\mu}{\sqrt{1+\mu^2}}\right)\right]\left[1 \pm \frac{\Delta P_0}{s\gamma_k f(\mu;\frac{s}{R})}\right]} \tag{8}$$

The discharge rate is defined as a product of the effective flow cross-section and the characteristic dynamic velocity of the granular medium. The effective area depends on outlet geometry and packing density, while the velocity term reflects the combined influence of gravity, interparticle friction, arch stability, and gas pressure effects. The mass flow rate of the granular medium is subsequently determined by integrating the effective outlet area and the material bulk density into Equation (9):

$$Z_t = 0.5\gamma_n \frac{\pi D_0^2}{4}\sqrt{2g\mu\left[R + s\left(0.5 + \frac{1-\mu}{\sqrt{1+\mu^2}}\right)\right]\left[1 \pm \frac{\Delta P_0}{s\gamma_k f(\mu;\frac{s}{R})}\right]} \tag{9}$$

A comparative analysis of experimental data with the results obtained using the proposed dependence in Equation (9) demonstrates high predictive accuracy, with calculated errors maintained within a narrow range of -28.6% to +28.9%.

To establish a more reliable method for determining the critical gas velocity W_{kr}, a comprehensive series of experiments was conducted on the cold scale model. The operational parameters were varied within the following ranges:

- Outlet diameter rate (D_0) 0.036-0.056 m;
- Equivalent particle diameter s_{eg} **:** from 0.001 to 0.005 m;
- Gas specific weight γ_r**:** from 1.2 to 9.2 N/m³;
- Bulk specific weight of material γ_k**:** from $14.5 \cdot 10^3$ to $43.5 \cdot 10^3$ to N/m³.
- g is the acceleration due to gravity. Its standard value is $g = 9.81$ m/s^2. It represents the acceleration of an object under the influence of Earth's gravitational force. In engineering and fluid mechanics calculations, g is commonly used in equations describing flow velocity, particle motion, and energy balance.

Based on the experimental results, specific dependencies were established, correlating the critical speed with the gas density, material properties, and particle dimensions. These findings provide a robust physical basis for preventing unpredictable material «hanging» or blockage in industrial systems. As a result of the experiments, the particular dependencies of the critical speed on the density of the gas, material and diameter of the piece were established. The theoretical basis for determining the critical gas velocity is founded on the hydrodynamic behavior of a gas flow passing through a granular porous medium. Under increasing gas velocity, the drag force exerted by the flowing phase on the particles gradually approaches the resisting forces associated with gravity, interparticle friction, and structural constraints of the granular bed. At the critical state, hydrodynamic instability occurs, leading to restructuring or partial fluidization of the granular layer. The derivation of the proposed correlations is based on dimensional analysis and empirical generalization of experimental results obtained for granular beds with different structural characteristics. The critical velocity may be expressed by Equation (10) as a function of the gas dynamic pressure and the structural parameters of the porous medium:

$$F_d \sim \rho_g W_{kr}^2 s_{eq} \tag{10}$$

where F_d is the drag force, ρ_g is the gas density, W_{kr} is the critical gas velocity, and s_{eq} is the equivalent flow cross-sectional area.

Assuming equilibrium between the aerodynamic forces and the resisting forces within the granular structure, the following dimensionless relationship can be defined by Equation (11):

$$W'_{kr} = \frac{1}{0.557\sqrt{\gamma_r}}, \tag{11}$$

where γ_r is the relative bulk density parameter.

Further transformation of the experimental data into generalized dimensionless coordinates yields Equation (12):

$$W''_{kr} = \sqrt{\frac{\gamma_k}{437}}, \tag{12}$$

which normalizes the critical velocity with respect to the structural coefficient of the granular medium, where γ_k characterizes the granular structure and accounts for porosity, particle arrangement, and internal flow resistance.

Analysis of the experimental datasets demonstrated an approximately linear dependence between the dimensionless critical velocity and the equivalent flow cross-sectional area. Consequently, the final empirical expression was expressed as Equation (13):

$$W'''_{kr} = \sqrt{\frac{s_{eq}}{0{,}0048} - 0.4} + 0.5\,. \tag{13}$$

The obtained equations therefore combine theoretical hydrodynamic considerations with experimental approximation and can be used to predict the onset of critical flow conditions in granular and porous media systems.

It has been established that the outlet diameter does not affect the critical velocity of the gas counterflow. The critical gas velocity was estimated using the following semi-empirical correlation derived from experimental approximation and torque-balance considerations by Equation (14):

$$W_{kr} = 0.087\sqrt{\frac{\gamma_k}{\gamma_r}}\left(\sqrt{\frac{s_{eq}}{0.048} - 0.4} + 0.5\right). \tag{14}$$

The regression analysis showed that the coefficient 0.087 provides the best agreement between calculated and experimental critical velocities within the investigated parameter range. The obtained correlation adequately reproduces the experimentally observed transition between stable discharge and blockage regimes. The predictive capability of the model was evaluated by comparing calculated and measured critical velocities. The deviation between experimental and calculated values did not exceed: -19.8% to +23.1% which is significantly lower than the deviations obtained using conventional empirical correlations.

The analysis confirms that the proposed relationship captures the combined influence of gas-dynamic conditions, granular structure, and effective flow geometry on the stability of dynamically unstable arches.

To further investigate the complex influence of gas dynamic parameters and the physical-mechanical properties of the granular medium, a series of experiments was conducted using volumetric models. The characteristics of the gases and materials used are detailed in Tables 2 and 4. A critical comparison with established empirical equations revealed significant discrepancies; traditional models exhibited errors ranging widely from -77.1% to +98.7%, +47.1% to +89.1%, and -60.1% to -73.7%.

These findings underscore that existing empirical correlations, largely derived from experiments involving only air flow, possess limited validity when applied to systems with varying gas properties. In contrast, our proposed model maintains high reliability across a broader spectrum of gas-dynamic conditions.

The dependence of the critical counter-current gas velocity W_{kr} on the gas specific weight γ_r is shown in Fig. 11.

To describe gas-assisted discharge of bulk materials, a unified semi-empirical framework was developed based on torque balance considerations and nonlinear regression analysis of experimental data.

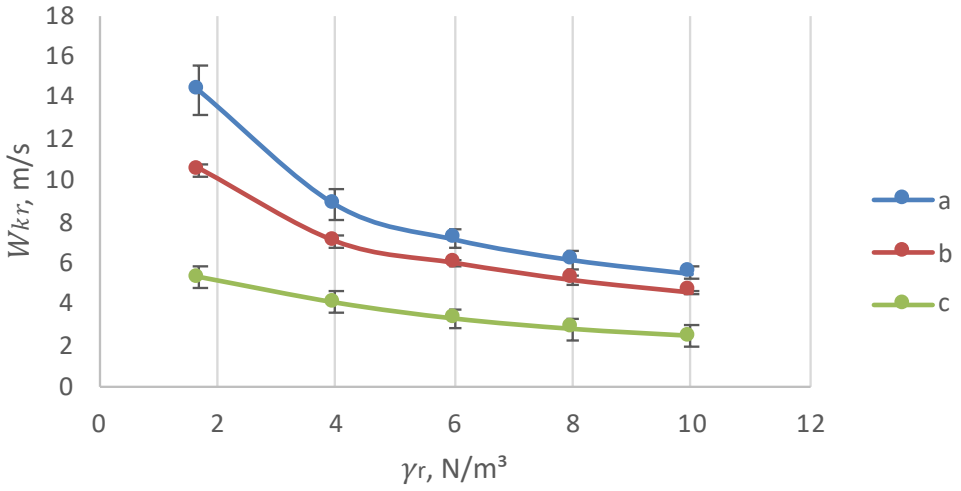

Fig. 11. Dependence of the critical velocity of the counter gas flow (W_{kr}, m/s) on its specific weight (γ_r, N/m³): (a) pellets II; (b) agglomerate III; (c) millet

The model couples two characteristic scales of the process:

- the critical gas velocity W_{kr}, defining the transition between stable and unstable discharge regimes by Equation (14);
- the macroscopic mass discharge rate Z_t, governing the global outflow rate is expressed by Equation (15):

$$Z_t = 0.5\sqrt{2g\mu\left[R + s\left(0.5 + \frac{1-\mu}{\sqrt{1+\mu^2}}\right)\right]\left[1 \pm \frac{\Delta P_0}{s\gamma_{kf}\left(\mu;\frac{s}{R}\right)}\right]}, \tag{15}$$

where gas pressure modifies the stability of dynamically unstable arch structures, resulting in either enhancement (+) or suppression (−) of discharge. The two relations are physically coupled through the same stability mechanism of dynamically unstable arches: W_{kr} defines the transition threshold at which gas flow destabilizes or stabilizes arch structures; Z_t describes the resulting macroscopic discharge response of the system. Thus, the condition $W \approx W_{kr}$ determines the transition between arch-controlled regime (low gas influence) and circulation-controlled regime (high gas influence). The proposed framework links microscopic stability conditions and macroscopic flow behavior through a torque-balance mechanism. Gas flow alters the equilibrium of forces acting on the arch structure, which simultaneously governs both the onset of instability and the resulting discharge intensity.

The model parameters were obtained using nonlinear least-squares regression, ensuring consistency between experimental measurements and theoretical predictions across the full range of investigated conditions.

It was observed that the material flow rate effectively reaches zero when the aerodynamic forces induce a state of «bulk material suspension» (hanging), where the upward gas pressure completely counteracts the gravitational and frictional forces within the arch structure. Equation (16)

$$1 - \frac{\Delta P_0}{s\gamma_{kf}\left(\mu;\frac{s}{R}\right)} = 0 \tag{16}$$

defines the critical balance between gas-induced forces and the structural resistance of the granular medium. By substituting the values of ΔP_0 and performing algebraic transformations, Equation (17) is obtained for the counter-current gas flow:

$$W_{kr} = m\sqrt{\frac{g \cdot s \cdot s_{eq}\gamma_{kf}\left(\mu;\frac{s}{R}\right)}{2\lambda H\gamma_r}}. \tag{17}$$

The governing equations are given by Equation (18) after substituting λ and R in Equation (17).

$$W_{kr} = m^{2-n}\sqrt{\frac{g^{1-n}s_{eq}^{1+n}\gamma_{kf}\left(\mu;\frac{s}{R}\right)}{2cH\gamma_r^{1-n}\eta^n}}. \tag{18}$$

The unstable turbulent regime of the counter-current gas flow ($c = 3.8; n = 0.2$) is described by Equation (19):

$$W_{kr} = m^{1.8}\sqrt{\frac{g^{0.8}s_{eq}^{1.2}\gamma_k f\left(\mu;\frac{s}{R}\right)}{7.6H\gamma_r^{0.8}\eta^{0,2}}}. \quad (19)$$

Under turbulent conditions (c=0.55, n=0) Equation (19) reduces to Equation (20)

$$W_{kr} = \sqrt{\frac{gs\cdot s_{eq}\gamma_k f\left(\mu;\frac{s}{R}\right)}{1{,}1H\gamma_r}}. \quad (20)$$

Assuming $s = s_{eq}$, the governing equation for the unstable turbulent regime takes the form represented by Equation (21).

$$W_{kr} = m^{1.8}\sqrt{\frac{g^{0.8}s^{2.2}\gamma_k f\left(\mu;\frac{s}{R}\right)}{7.6H\gamma_r^{0.8}\eta^{0.2}}\cdot\left[\frac{4m}{k(1-m)}\right]^{1.2}} \quad (21)$$

and for the turbulent regime it is expressed as Equation (22)

$$W_{kr} = ms\sqrt{\frac{g\gamma_k f\left(\mu;\frac{s}{R}\right)}{1{,}1H\gamma_r}\cdot\frac{4m}{k(1-m)}} \quad (22)$$

The accuracy of the developed analytical models was rigorously tested against experimental data. A comparison of the critical velocities for counter-current gas flow calculated using Equation (21) shows satisfactory agreement, with errors ranging from -36.5% to +17.0%. Equation (21) provided an accuracy ranging from -25.6% to -35.0% and from -26.3% to -38.4% for the respective series. Further refinement in Equation (22) allowed for a significant reduction in the error margin to a range of -13.8% to +28.7% (as shown in Fig. 10).

This enhanced precision is attributed to the model's ability to account for the intense turbulence of the gas phase within the granular bed, which becomes particularly pronounced just before flow blockage occurs. At the same time, the error for the critical velocities of the oncoming air flow, calculated using Equation (22), is reduced to a range of -19.6 to -30.1% and from -18.1 to -32.4% accordingly. This is explained by the significant turbulence of the gas flow in the layer, especially prior to the onset of flow blockage.

The reliability of these calculations was confirmed across a broad experimental range:

- Gas properties: Specific gravity from 11.96 to 1.16 N/m³; dynamic viscosity from $8.9\cdot10^{-6}$ to $1.81\cdot10^{-5} Pa\cdot s$
- Material properties: Particle diameter from 0.5 to 15.0 mm; bulk density from 14.2 to 39.1 kN/m³; internal friction coefficient from 0.55 to 0.95.
- Geometric parameters: Outlet diameter from 0.01 to 0.065 m; d/R ratio from 0.02 to 0.4.

Thus, analytical Equation (17) significantly improves the accuracy of calculating the critical velocity of a counter-current gas flow and makes it possible to evaluate the influence of gas parameters, the physical and mechanical properties of the bulk material, and the outlet size. Analysis of Equation (21) identifies the equivalent diameter, material density, internal friction, and particle shape as the dominant factors influencing the mass discharge rate. In contrast, gas viscosity and outlet diameter exert minimal influence on the outflow rate.

A critical finding of this study is the shift in factor significance during the transition to a turbulent counter-current flow. As the system approaches the blockage limit, the influence of gas density increases substantially. Concurrently, the impact of bed porosity, particle size, and shape decreases, while the role of gas viscosity practically disappears. This confirms that at high velocities, the aerodynamic drag acting on the arch structure becomes the primary governing force.

The developed analytical model (Equation 17) is universal and demonstrates high accuracy in predicting the critical velocity of counter-current gas flows. It effectively integrates the influence of outlet geometry, solid-phase characteristics, and gas-dynamic parameters. This provides a robust tool for the design and optimization of bulk material flow in horizontal-plane discharge systems, ensuring stable operation in industrial metallurgical furnaces.

4. Discussion

4.1. Mechanistic interpretation of gas-solid discharge

The results of this study demonstrate that the discharge of bulk material under gas-solid interaction is governed by the stability of dynamically formed arch structures. These arches act as temporary load-bearing configurations that control the continuity of flow and determine whether the system exhibits stable discharge, intermittent blockage, or circulation-dominated transport.

A key outcome of the present work is the identification of a unified regime structure governed by the critical gas velocity W_{kr}. The proposed model shows that discharge behavior is controlled by the balance between gravitational driving forces, internal friction, gas dynamic dissipation, and structural resistance of the granular assembly.

4.2. Arch stability mechanism

The formation and collapse of arches is governed by a torque equilibrium condition acting on particle clusters. When gas-induced forces exceed the structural resistance of the granular network, the arch becomes unstable and collapses, resulting in enhanced discharge. Conversely, when resistance dominates, stable blockage occurs.

This mechanism provides a physically consistent explanation for the observed transition between flow regimes and extends classical empirical descriptions of granular discharge.

4.3. Role of gas dynamics

The analysis shows that gas flow plays a dual role depending on the regime:

- In the arch-controlled regime, gas stabilizes or destabilizes granular structures depending on flow direction and pressure distribution;
- In the turbulent regime, gas promotes circulation zones that suppress arch formation and enhance continuous discharge.

This behavior is captured by the dimensionless pressure parameter embedded in the governing equations.

4.4. Regime transition

The results confirm the existence of a critical transition condition $W \approx W_{kr}$. At this threshold, the system transitions from intermittent arch-controlled discharge to circulation-controlled continuous flow.

This transition represents a fundamental change in the internal structure of the flow field. At low gas velocities, the discharge process is governed by intermittent arch formation and collapse, resulting in a non-continuous flow regime. With increasing gas velocity, a transition occurs toward a circulation-dominated regime, where persistent arch structures are suppressed and continuous material transport is established.

4.5. Comparison with previous studies

Classical models of granular discharge, such as empirical scaling laws, primarily describe gravity-driven flow and do not explicitly account for internal structural dynamics or gas-solid coupling effects. In contrast, the present study introduces a mechanistic framework based on arch stability and torque balance, enabling explicit prediction of regime transitions under varying gas dynamic conditions.

4.6. Model implications

The proposed unified model integrates laminar, transitional, and turbulent regimes within a single framework. It demonstrates that macroscopic discharge behavior can be directly linked to microstructural stability conditions of granular arches.

The results provide a predictive tool for controlling industrial processes such as pneumatic conveying, hopper discharge, and gas-assisted transport systems.

4.7. Combination of key findings

The main contributions of this study can be summarized as follows:

- Identification of arch-controlled and circulation-controlled regimes;
- Definition of a critical velocity W_{kr} governing regime transition;
- Development of a unified semi-empirical model combining geometry, gas dynamics, and granular structure;
- Experimental confirmation of predicted discharge behavior across a wide parameter range.

5. Conclusions

To investigate gas-solid interaction effects on bulk material discharge through a horizontal outlet, a combined experimental and theoretical study was conducted. The influence of gas flow direction on arch stability and flow regime transitions was analyzed. The main findings are summarized below:

1. The discharge process is governed by the cyclic formation and collapse of dynamically unstable arches. Gas flow direction plays a key role in controlling arch stability. Under co-current gas flow conditions, arch destabilization enhances discharge, increasing the relative flow rate up to $Z_t/Z_0 = 1.45$, whereas counter-current gas flow stabilizes arch structures and reduces the discharge rate to 0.2-0.6 Z_0, leading to blockage at critical gas velocities.
2. Two distinct flow regimes were identified: an arch-controlled regime at low and moderate gas velocities, characterized by intermittent arch collapse, and a circulation-controlled regime at higher gas velocities, where the formation of a stable circulation zone above the outlet fundamentally changes the discharge mechanism.
3. The proposed torque-balance model provides a physically based description of arch stability under gas-solid interaction conditions and demonstrates improved predictive capability compared with conventional empirical correlations.
4. The developed approach is applicable to the design and optimization of industrial bulk handling systems, including pneumatic conveying units and shaft furnaces.

The present study was carried out under controlled laboratory-scale conditions, which allowed systematic analysis of gas-solid interaction effects within well-defined ranges of particle size, outlet geometry, and gas velocity. The obtained results provide a consistent basis for understanding the observed flow regimes; however, extension to industrial-scale systems and fully coupled CFD-DEM simulations may further improve the generality and predictive capability of the proposed approach.

Acknowledgments

This study was supported by the grant AP23486482 from the Science Committee of the Higher Education and Science Ministry of the Republic of Kazakhstan.

References

ALONSO-MARROQUIN, F., MORA, P. 2021. *Beverloo law for hopper flow derived from self-similar profiles.* Granular Matter. 23, 7.

AMANBAEV, T.R., ANTONY, S.J. 2022. *Modeling the outflow of particulate solids from a container considering wall adhesion.* Fluid Dynamics. 57, 954–966.

BANIK, R.K., DAS, H.J. 2024. *MFIX–DEM simulation of gas–solid flow in dual fluidized bed system*. IOP Conference Series: Earth and Environmental Science. 1372, 012100.

BARLETTA, D., DONSÌ, G., FERRARI, G., POLETTO, M. 2003. *On the role and the origin of the gas pressure gradient in the discharge of fine solids from hoppers.* Chemical Engineering Science. 58, 5269–5278.

BEMBENEK, M., DMYTRIV, V., BANHA, V., HORODNIAK, R., PAWLIK, J. 2024. *A Mathematical Model for Conical Hopper Mass Efficiency*. Applied Sciences. *14*(16), 7373.

CHEN, J., GE, M., LI, L., ZHENG, G. 2023. *Material transport and flow pattern characteristics of gas–liquid–solid mixed flows.* Processes. 11, 2254.

CHEN, K., WANG, H., WANG, X. 2024. *Numerical simulation of gas–solid flow processes in an ash conveying pipeline with multiple feeds*. Fluid Dynamics & Materials Processing. 20, 2721–2739.

CHU, K., CHEN, Y., JI, L., ZHOU, Z., YU, A., CHEN, J. 2022. *Coarse-grained CFD–DEM study of gas–solid flow in gas cyclone.* Chemical Engineering Science. 260, 117906.

FENG, Y., YUAN, Z. 2021. *Discrete element method modeling of granular flow characteristics transition in mixed flow*. Computational Particle Mechanics. 8, 21–34.

GUO, C., LIU, G., WANG, X. 2026. *CFD-DEM coupling analysis of EPB screw conveyor muck discharge in water-rich sandy cobble strata*. Scientific Reports. 16, 12407.

HANIF, M., MAZA, D., VAN DER MEER, D. 2025. *Effect of particle shape on the discharge from a mono-layer hopper*. Granular Matter. 27, 43.

HARRIS, D., GREKOVA, E. 2005. *A hyperbolic well-posed model for the flow of granular materials*. Journal of Engineering Mathematics. 52, 107–135.

HUANG, H., ZHANG, Y., WANG, D., FU, Z., TIAN, H., SHANG, J., HELAL, M., LV, Z. 2024. *Study the Flow Capacity of Cylindrical Pellets in Hopper with Unloading Paddle Using DEM.* Agriculture. 14(4), 523.

KOBYŁKA, R., WIĄCEK, J., PARAFINIUK, P., HORABIK, J., BAŃDA, M., STASIAK, M., MOLENDA, M. 2021. *Discharge Flow of Spherical Particles from a Cylindrical Bin: Experiment and DEM Simulations*. Processes. 9(11), 1860.

LI, T., DELSMAN, E., PANNALA, S. 2026. *Mass flow rate prediction for gas-controlled hopper discharge of free-flowing granular materials*. Powder Technology. 473, 122190.

LU, Y., JIANG, Z., ZHANG, X., E, D. 2024. *Solid flow in an experimental oxygen blast furnace model: effects of recycled gas and raceway*. Energies. 17, 309.

MA, H., ZHOU, L., LIU, Z., CHEN, M., XIA, X., ZHAO, Y. 2022. *A review of recent developments for CFD–DEM investigations of non-spherical particles.* Powder Technology. 412, 117972.

MANKOC, C., JANDA, A., ARÉVALO, R., PASTOR, J., ZURIGUEL, I., GARCIMARTIN, A., MAZA, D. 2007. *The flow rate of granular materials through an orifice*. Granular Matter. 9, 407–414.

QIU, Z., XIAO, Q., YUAN, H., HAN, X., LI, C. 2024. *Particle shape and clogging in fluid-driven flow: A coupled CFD–DEM study*. Powder Technology. 402, 119566.

SCHEFFLER, O., COETZEE, C. 2023. *Discrete Element Modelling of a Bulk Cohesive Material Discharging from a Conveyor Belt onto an Impact Plate*. Minerals. 13(12), 1501.

SUN, D., LIU, P., HUI, S., YAN, T., SONG, N. 2025. *Experimental Study on the Mass Flow Rate Characteristics of a Fluidized Bed Powder Fuel Feeding System.* Powder Technology. 449, 120351.

TANG, X., SHEN, Y. 2024. *A bilateral semi-resolved CFD-DEM approach for cost-effective modelling in a rotary drum*. Chemical Engineering Science. 299, 120491.

WANG, C., LI, W., LI, B., JIA, Z., JIAO, S., MA, H. 2023. *Study on the influence of different factors on pneumatic conveying in horizontal pipe.* Applied Sciences. 13, 5483.

WANG, S., SHEN, Y. 2025. *CFD-DEM modelling of dense gas-solid reacting flow: Recent advances and challenges*. Progress in Energy and Combustion Science. 109, 101221.

WANG, Y., WILLIAMS, K., JONES, M., CHEN, B. 2017. *CFD simulation methodology for gas-solid flow in bypass pneumatic conveying – a review.* Applied Thermal Engineering. 125, 185–208.

WU, Y., ZHENG, Q., ZHU, H., YU, A. 2024. *Micro–macro constitutive relationship for solid phase pressure in hopper flows.* Powder Technology. 434, 119268.

XIAO, F., LUO, M., HUANG, F., ZHOU, M., AN, J., KUANG, S., YU, A. 2023. *CFD–DEM investigation of gas-solid flow and wall erosion of vortex elbows conveying coarse particles*. Powder Technology. 424, 118524.

XIE, Z., WANG, S., SHEN, Y. 2021. *CFD-DEM modelling of the migration of fines in suspension flow through a solid packed bed*. Chemical Engineering Science 231, 116261.

XU, D., LI, Y., XU, X., ZHANG, Y. 2026. *Particle Movement Mechanism of Wheat Particles in a 90° Bend of a Pneumatic Conveying System*. Processes, 14(5), 857.

XU, T., ZHOU, H., ZHANG, Y., ZHANG, T., HUANG, J., CAI, H., KOU, M., WU, .2024. *Numerical simulation of hydrogen-enriched shaft furnace.* International Journal of Hydrogen Energy. 55, 1131–1142.

YANG, S.-C., HSIAU, S.-S. 2001. *The simulation and experimental study of granular materials discharged from a silo with the placement of inserts.* Powder Technology. 120, 244–255.

ZHANG, X., YU, Y., HU, Y. 2022. *Experimental study on gas–liquid–solid interaction characteristics in the launch tube*. Journal of Marine Science and Engineering. 10, 1239.

ZHANG, X., ZHAO, C., GE, H., LIU, Z., LIU, Y., JIAO, L. 2024. Analysis of gas-solid flow characteristics in intricate pipelines. Chemical Engineering Research and Design. 204, 438-449.

ZHANXIA, D., YAN, B., HUANG, M., CHENG, B. 2025. *Numerical simulation of reduction behavior in shaft furnace based on DEM and CFD.* International Journal of Chemical Reactor Engineering. 23, 373–391.

ZHOU, H.; XU, K.; TIAN, X.; KOU, M.; WU, S.; SHEN, Y. 2021. *Influence of burden profile on gas-solid distribution in COREX shaft furnace with center gas supply by CFD-DEM model*. Powder Technology. 392, 672–679.

ZHU, Z.; ZHOU, P.; CHEN, Z.; WU, D.; KUANG, S. 2024. *CFD–DEM modeling of particle segregation behavior in a simulated flash smelting furnace*. Powder Technology. 448, 120310.